

# Reconfigurable inverse designed phase-change photonics

Changming Wu<sup>1</sup>, Ziyu Jiao<sup>1</sup>, Haoqin Deng<sup>1</sup>, Yi-Siou Huang<sup>2,3</sup>, Heshan Yu<sup>2,3</sup>, Ichiro Takeuchi<sup>3</sup>, Carlos A. Ríos Ocampo<sup>2,3</sup> and Mo Li<sup>1,4,\*</sup>

<sup>1</sup>Department of Electrical and Computer Engineering, University of Washington, Seattle, WA 98195, USA

<sup>2</sup>Department of Materials Science and Engineering, University of Maryland, College Park, MD 20742, USA

<sup>3</sup>Institute for Research in Electronics and Applied Physics, University of Maryland, College Park, MD 20742, USA

<sup>4</sup>Department of Physics, University of Washington, Seattle, WA 98195, USA

## Abstract

**Integrated photonic network-on-chip (NoC) fabrics can provide multiple terabits per second (Tbps) bandwidth for high-performance computing servers supporting the latest artificial intelligence. To maximize the utility of the photonic hardware, these optical networks can multiplex data streams in multi-dimensional channels encoded in optical wavelengths, modes, and polarization states. A generic photonic platform that can be reconfigured to implement functionalities in those dimensions is highly desirable to streamline the design and manufacturing of integrated photonic networks. Here, we demonstrate a multi-functional photonic device using phase-change material  $\text{Sb}_2\text{Se}_3$  that can be reconfigured from a wavelength-division demultiplexer to a mode-division demultiplexer. The reconfiguration is achieved by direct laser writing of phase patterns optimized with the inverse design technique. The demonstrated programmable phase-change photonic devices hold immense promise for a wide range of photonic applications requiring adaptable functionalities, including on-chip and in-package optical interconnects, optical signal processing, photonic tensor cores, and future optical computing for artificial intelligence.**

---

\* Corresponding author: moli96@uw.edu

## Introduction

Recent advancements in large-scale photonic integrated circuits have unveiled the potential of in-package and on-chip optical networks<sup>1-4</sup> that affords a remarkable leap in bandwidth density compared to traditional electrical interconnects and networks. This advancement paves the way for unprecedented bandwidth and energy efficiency for communications among crucial system components like processors, memory modules, and storage units<sup>5</sup>, potentially transforming the architecture of high-performance computing systems<sup>4</sup> and data centers<sup>5</sup> for the advent of artificial intelligence (AI), especially the generative type. In today's integrated photonic systems, programmability and reconfigurability stand as highly desired features, essential for empowering diverse technologies—from next-generation data centers<sup>6,7</sup> to optical neural networks<sup>8-12</sup> and quantum information processing<sup>13-17</sup>. Within this context, the development of an on-chip, high-density photonic network fabric allowing dynamic reconfiguration emerges as a pivotal element<sup>18</sup>. An exemplary instance is the Google TPU v4, employing MEMS-based optical circuit switches to configure the interconnect topology, thereby enhancing scalability and power efficiency in machine learning models<sup>19</sup>. Such a network-on-chip fabric plays a vital role in effectively managing data flow across various functional units within the system<sup>20</sup>. A key building block in creating this fabric is a multi-functional photonic device enabling post-fabrication programming, an immensely desired capability for agile reconfigurable photonic functionalities. However, conventional programmable photonics devices such as phase shifters, directional couplers, and beam splitters based on Mach-Zehnder interferometers (MZIs) have limitations: while programmable in operational parameters, their functionality is hardcoded and cannot be changed. Therefore, new devices with modifiable functionality will provide even greater flexibility in adjusting the configuration and topology of the photonic network to optimize it for various algorithms and thus are highly desirable.

Chalcogenide phase-change materials (PCMs) present a promising solution to realize programmable photonics due to their nonvolatile, reversible microstructural phase transition, the ability for multilevel operation, and significant refractive index contrast between phases<sup>21-23</sup>. PCMs, including  $\text{Ge}_2\text{Sb}_2\text{Te}_5$ , GSST,  $\text{Sb}_2\text{Se}_3$ , or  $\text{Sb}_2\text{S}_3$ , have been incorporated in Mach-Zehnder interferometers (MZIs)<sup>24,25</sup> and directional couplers<sup>26,27</sup> for phase modulation and in ring resonators for resonance tuning<sup>28,29</sup>. In these applications, the PCMs are only used to tune the

photonic devices' parameters rather than changing their functionalities, which should be possible considering the very high optical index contrast afforded by PCMs. Moreover, a variety of sophisticated design optimization techniques can be implemented in PCM-integrated photonic devices to enable programmability. These methods include genetic algorithms<sup>30,31</sup>, semi-analytical approaches<sup>32,33</sup>, and notably, inverse design<sup>34,35</sup>. Inverse design, in particular, has expanded the exploration of design spaces, yielding devices with exceptionally compact footprints and superior performance metrics<sup>36</sup>.

In this study, we present a reprogrammable, multi-functional photonic device achieved by integrating the low-loss phase-change material,  $\text{Sb}_2\text{Se}_3$ , on a multi-mode interferometer (MMI). Employing the direct laser writing technique in conjunction with inverse design optimization, we modify the device's functionality by transferring the inverse-designed phase pattern to the  $\text{Sb}_2\text{Se}_3$  thin film while preserving the integrity of other components. Remarkably, the functionality of this phase-change MMI device is rewritable, allowing for the erasure and recreation of the  $\text{Sb}_2\text{Se}_3$  phase pattern. This capability completely transforms the device's functionality, making it adaptable to different application scenarios. As a demonstration, we successfully programmed this device to function as a wavelength-division multiplexing (WDM) device and subsequently changed it into a mode-division multiplexing (MDM) device. This result showcases the ability of phase-change photonic devices to enable flexible integrated photonic circuits for multi-dimensional communication schemes, switchable or combining wavelength- and mode-multiplexing functionalities.

## Results

Figure 1a illustrates the schematic of the proposed reconfigurable multi-functional  $1 \times 2$  MMI. Each MMI, occupying a footprint of  $40 \times 8.5 \mu\text{m}^2$ , is fabricated on a 330 nm-thick  $\text{Si}_3\text{N}_4$ -on-insulator substrate. A 30 nm-thick low-loss phase-change material,  $\text{Sb}_2\text{Se}_3$ , is sputtered onto the MMI and protected by a 200 nm-thick  $\text{SiO}_2$  capping layer. The significant refractive index contrast between the two phases of  $\text{Sb}_2\text{Se}_3$  (amorphous:  $n_a = 3.285$  and crystalline:  $n_c = 4.050$ , respectively) allows efficient evanescent coupling of light within the MMI with the  $\text{Sb}_2\text{Se}_3$  thin film. As a result, the light undergoes a phase modulation that depends on the local structure of  $\text{Sb}_2\text{Se}_3$ . By inducing localized perturbations, the phase pattern of  $\text{Sb}_2\text{Se}_3$  on MMI shapes the wavefront during light

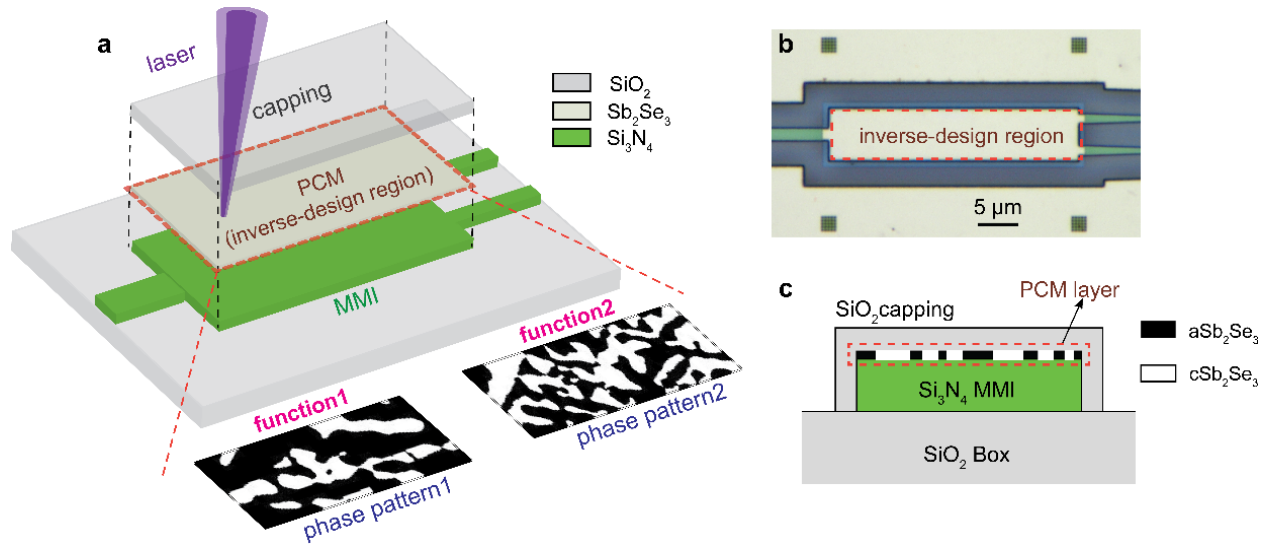


**Figure 1 Schematic of the laser writing of multi-functional photonic MMI.** **a.** Illustration of programming a  $\text{Sb}_2\text{Se}_3$  thin film integrated MMI using a focused laser beam. The commercial direct laser writing system (Heidelberg DWL66+) is used to write/erase various phase patterns onto the  $\text{Sb}_2\text{Se}_3$  thin film, which determines the function of the MMI. **b.** The top-view optical image of an as-fabricated  $40 \times 8 \mu\text{m}^2$  MMI. The device’s functionality is defined by the  $\text{Sb}_2\text{Se}_3$  phase pattern in the “inverse design region” (red dashed box). **c.** The cross-sectional schematic of the MMI device with patterned  $\text{Sb}_2\text{Se}_3$ . To change the function of the device, the phase pattern in the  $\text{Sb}_2\text{Se}_3$  thin film is recreated, while all the other components remain unchanged.

propagation, altering the amplitude and phase distribution of the propagating light. This capability allows the MMI to execute diverse functions with minimum loss penalty. In particular, we can associate the specific function of the MMI device with a distinct binary  $\text{Sb}_2\text{Se}_3$  phase pattern within the “inverse-design region” highlighted by the red dashed box in Figure 1b. Furthermore, as depicted in Figure 1c, the MMI’s function is entirely encoded within the PCM thin film, while the other components remain unchanged. The reversible phase change of  $\text{Sb}_2\text{Se}_3$  allows for convenient erasure and recreation of the phase pattern, enabling a complete transformation of the device’s functionality to cater to vastly different application scenarios.

Programming the MMIs involves designing and patterning processes. First, we determine the MMI’s function and design the corresponding  $\text{Sb}_2\text{Se}_3$  phase pattern. To achieve this, we employ a topology optimization approach to inverse-design the phase pattern of the  $\text{Sb}_2\text{Se}_3$  thin

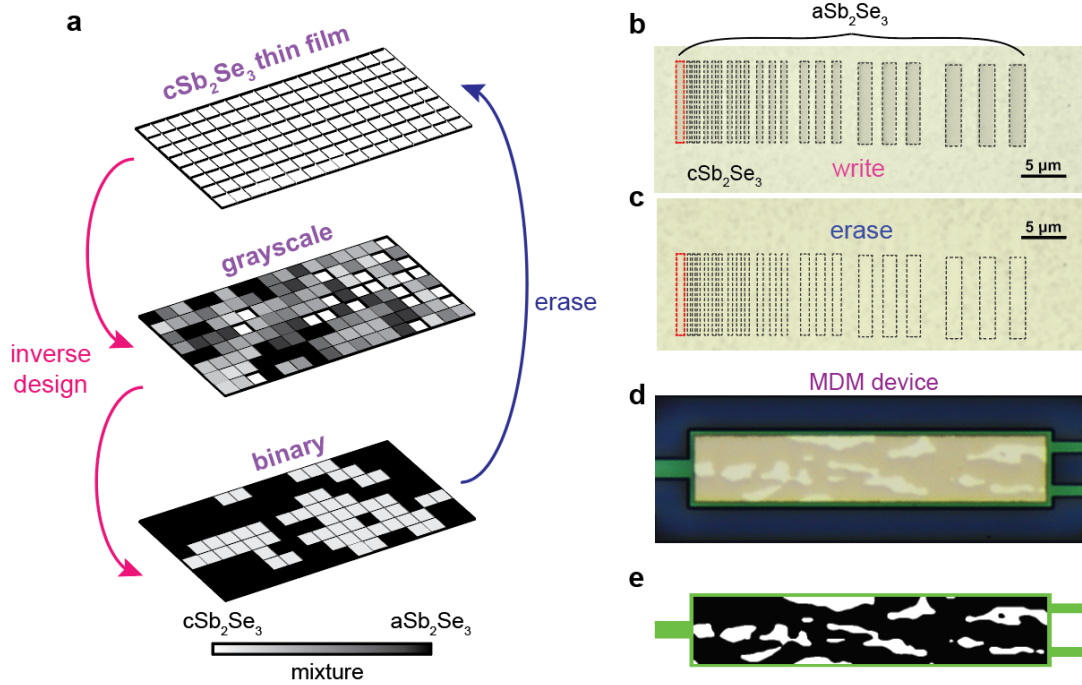


**Figure 2 Inverse design of the  $\text{Sb}_2\text{Se}_3$  phase pattern.** **a.** Schematic of the inverse design approach to generate phase pattern for the  $\text{Sb}_2\text{Se}_3$  MMI. The optimization is initiated with a fully crystalline  $\text{Sb}_2\text{Se}_3$  thin film, and then the amorphous-crystalline spatial distribution is inverse-designed using the topology optimization method, resulting in a binary phase pattern. White and black areas indicate the crystalline and amorphous  $\text{Sb}_2\text{Se}_3$ , respectively. **b.** Optical image of  $\text{aSb}_2\text{Se}_3$  rectangular array written on  $\text{cSb}_2\text{Se}_3$  thin film for testing the writing resolution. The minimum feature size achieved is 300 nm. **c.** The test pattern in **(b)** is erased back to the  $\text{cSb}_2\text{Se}_3$  phase by thermal annealing. The area marked by dashed lines indicates the initial patterns. **d.** Optical images of an inverse-designed pattern for the mode demultiplexer written in  $\text{Sb}_2\text{Se}_3$ . **e.** The corresponding inverse designed, binarized  $\text{Sb}_2\text{Se}_3$  phase pattern for the mode demultiplexer.

film<sup>37,38</sup>. In our simulations, we segment the  $\text{Sb}_2\text{Se}_3$  thin film within the “inverse-design region” into an array of pixels, each measuring  $100 \text{ nm} \times 100 \text{ nm} \times 30 \text{ nm}$ , while maintaining the other components of the MMI unchanged during optimization. To avoid unachievably fine features, we also limit the minimum feature size in the designed patterns to be larger than 500 nm. The optimization process initiates with a linear parametrization, allowing the dielectric permittivity  $\epsilon_i$  of each pixel to continuously vary in the range of  $(n_a, n_c)$ . Subsequently, the phase pattern is updated using the steepest descent method. Through this gradual optimization process, the permittivity of the pixels transitioned from an intermediate value in  $(n_a, n_c)$  toward a binary value

of  $n_a$  or  $n_c$ . Consequently, the phase map evolved from a grayscale phase pattern to the binary phase pattern of  $\text{Sb}_2\text{Se}_3$ , as illustrated in Figure 2a.

Second, the corresponding phase pattern is directly laser written onto the MMIs using a commercial 405 nm laser direct lithography system (Heidelberg DWL 66+, 405 nm laser). The exceptional speed and accuracy of the DWL system enable efficient and effective patterning of the target MMI device. During the experiment, we began with the  $\text{Sb}_2\text{Se}_3$  thin film in the completely  $\text{cSb}_2\text{Se}_3$  phase and wrote phase patterns directly onto the MMI by quenching  $\text{cSb}_2\text{Se}_3$  into  $\text{aSb}_2\text{Se}_3$  phase using optical heating<sup>39,40</sup>. Figure 2b displays a series of rectangular  $\text{aSb}_2\text{Se}_3$  patterns with widths ranging from 200 nm to 2  $\mu\text{m}$  written on a blank  $\text{cSb}_2\text{Se}_3$  film, demonstrating a minimum feature size of  $\sim 300$  nm achieved through laser writing. We note that this resolution reaches the subwavelength regime and is much smaller than the resolution achieved in previous works<sup>39,41,42</sup>. Furthermore, the pattern can be readily erased through an annealing process, either by local heating using a continuous-wave laser or global heating to 180 °C using a hotplate (see Figure 2c). By selectively erasing and rewriting the patterns on MMIs, the function of the circuit is reprogrammed. This technique gives us a toolkit for writing high-finesse functional patterns into the phase-change films and modifying or erasing them as required.

Using the direct writing technique, we first demonstrate programming the MMI as a mode demultiplexer (MDM). The  $\text{Sb}_2\text{Se}_3$  phase pattern (Figure 2e), generated with the inverse design approach, was precisely aligned (misalignment  $< 125$  nm) and written onto the MMI. As shown in Figure 2d, the laser-written phase pattern closely resembles the design with minimal error. Subsequently, we characterized the MDM performance of the MMI device. Figure 3a shows an optical microscope image of the complete photonic circuit and a sketch of the measurement setup. A multimode waveguide, supporting both  $\text{TE}_0$  and  $\text{TE}_1$  modes, is connected to the input of the MMI, while both output ports (port 2 and port 3) are linked to single-mode waveguides for measurement. The incident light is coupled to the device via either port 1 or port 4 and passes through a mode combiner constructed with an asymmetric directional coupler. This combiner selectively converts the incoming  $\text{TE}_0$  mode from incident port 4 to the  $\text{TE}_1$  mode while maintaining the  $\text{TE}_0$  mode from input port 1. The design and characterization of the mode combiner is included in Supplementary Information. As a result, the input mode to the MMI is determined based on which port is used (port 1 for  $\text{TE}_0$  or port 4 for  $\text{TE}_1$ ), which is selected using a  $1 \times 2$  optical

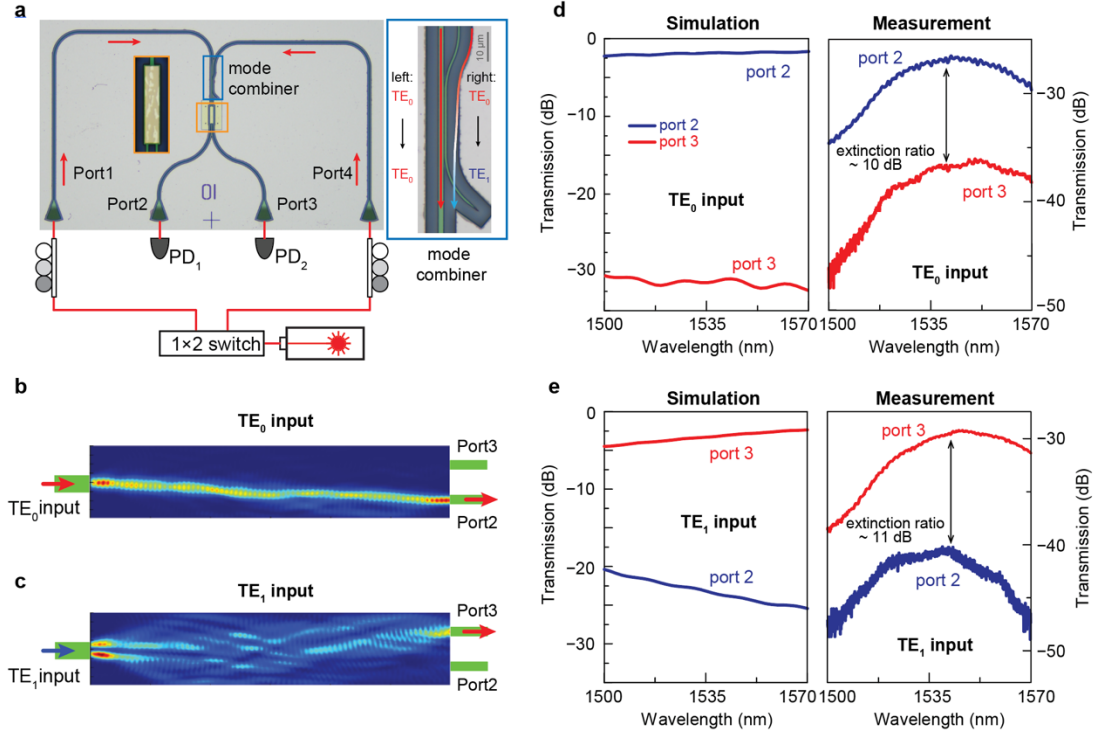


**Figure 3. MMI programmed as a mode demultiplexer.** **a.** The optical setup for the MDM device measurement. An optical switch and a mode combiner control the input mode,  $TE_0$  or  $TE_1$ , to the MDM. Inset: the optical image of the mode combiner. **b.** and **c.** The simulated  $|E|^2$  distribution in the MDM with  $TE_0$  mode input (**b**) and  $TE_1$  mode input (**c**) at the wavelength of 1550 nm. **d** and **e.** The simulated (left column) and measured (right column) transmission spectrum of the mode demultiplexer when the  $TE_0$  mode (**d**) or  $TE_1$  mode (**e**) is input. The lower extinction ratio is attributed to fabrication imperfections and laser writing misalignment.

switch. Finally, the output power from both output ports (port 2 and port 3) was measured to determine the respective transmission coefficients of each mode.

Figures 3b and 3c illustrate the MDM's functionality, routing the  $TE_0$  mode to port 2 and the  $TE_1$  mode to port 3 over a wavelength range of 1500 to 1600 nm. Figures 3d and 3e compare the simulated and measured transmission spectra of the two modes. In the simulation, this MDM device demonstrates a modal extinction ratio surpassing 15 dB for both mode channels over a bandwidth wider than 100 nm. The experimental results exhibit an extinction ratio of  $> 10$  dB for both mode channels, lower than the simulated values. We attribute the underperformance to fabrication imperfections, misalignment, and roughness in the phase pattern. Additionally, in our

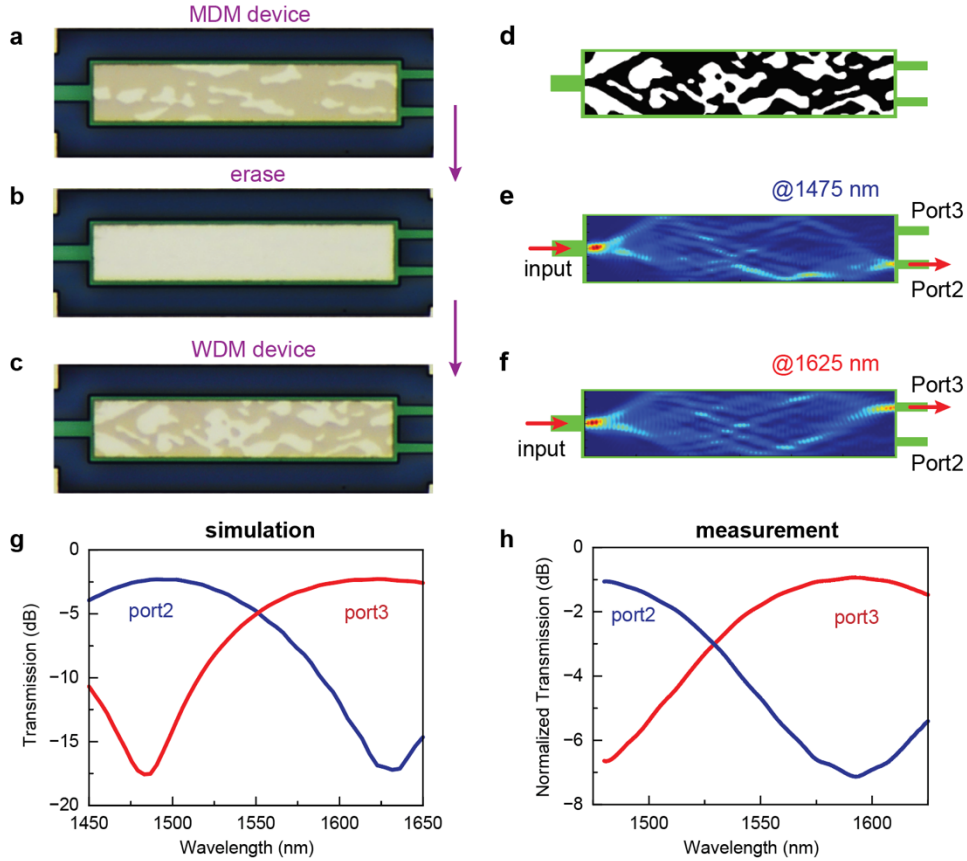


**Figure 4 Reprogramming to a wavelength demultiplexer. a to c.** Optical images showing the steps that the MDM device (a) is first erased to the full crystalline  $\text{cSb}_2\text{Se}_3$  thin film (b) and then reprogrammed as a WDM (c). **d.** Inverse-design binarized  $\text{Sb}_2\text{Se}_3$  phase pattern for the WDM. White and black areas indicate the crystalline and amorphous  $\text{Sb}_2\text{Se}_3$ , respectively. **e and f.** Simulated  $|E|^2$  distribution of the WDM device operating at 1475 nm (e) and 1625 nm (f). **g and h.** Transmission spectra to output ports 2 and 3 obtained from simulation (g) and measurement (h).

measurements, the grating couplers constrain the insertion loss and operational bandwidth. Furthermore, we fabricated three identical devices, which demonstrated similar performance (see Supplementary Information), manifesting the consistency of the design and fabrication approach.

We then demonstrate reprogramming the functionality of the MMI from an MDM to a wavelength demultiplexer (WDM). To do so, we erased the previous  $\text{Sb}_2\text{Se}_3$  phase pattern and rewrote a newly designed phase pattern onto the same MMI, as shown in Figures 4a to 4c. To accomplish the WDM function, we redesigned the phase pattern within the “inverse-design region” using the same method described earlier (Figure 4d). Figures 4e and 4f show the simulated electric



field distribution at two operating wavelengths of 1475 nm and 1625 nm, respectively. The WDM separates the  $TE_0$  mode of the input waveguide into the two output ports according to their wavelength: 1475 nm at port 2 and 1625 nm at port 3. Figures 4g and 4h plot the measured and simulated transmission spectra for the WDM, respectively. The simulation shows a high extinction ratio of  $> 15$  dB at the center wavelengths. The experimental results show a lower extinction ratio of  $>6$  dB measured at wavelengths of 1465 nm and 1695 nm, which is limited by the range of the tunable laser source used. The reduced performance can again be attributed to fabrication imperfections and pattern misalignment. Nevertheless, the results successfully demonstrate a complete change of the device's functionality, from an MDM to a WDM, by recreating the phase pattern of the  $Sb_2Se_3$  thin film.

## **Conclusion**

In summary, our work demonstrates the versatility of a multi-functional photonic device achieved through the integration of low-loss phase-change material  $Sb_2Se_3$  onto a silicon nitride photonic integrated circuit, where functionality is encoded in the phase pattern of the  $Sb_2Se_3$  thin film. Leveraging direct laser writing and inverse design optimization, this novel phase-change MMI device offers excellent flexibility for a single photonic device. We successfully programmed this device to operate as multiplexers for either wavelengths or spatial modes. Utilizing photonic inverse design ensured high extinction ratios and broadband response in both configurations. Moreover, there is potential for further exploration of the application scenario by adopting a multi-level grayscale design instead of the current binary design and cascading multiple stages of such photonic structures to enable a diverse range of complex reconfigurable photonic systems.

## Reference

1. Shacham, A., Bergman, K. & Carloni, L. P. Photonic networks-on-chip for future generations of chip multiprocessors. *IEEE Transactions on Computers* **57**, 1246–1260 (2008).
2. Stojanović, V. *et al.* Monolithic silicon-photonics platforms in state-of-the-art CMOS SOI processes. *Opt Express* **26**, 13106–13121 (2018).
3. Atabaki, A. H. *et al.* Integrating photonics with silicon nanoelectronics for the next generation of systems on a chip. *Nature* **556**, 349–353 (2018).
4. Yang, K. Y. *et al.* Multi-dimensional data transmission using inverse-designed silicon photonics and microcombs. *Nat Commun* **13**, 7862 (2022).
5. Sun, C. *et al.* Single-chip microprocessor that communicates directly using light. *Nature* **528**, 534–538 (2015).
6. Nikolova, D. *et al.* Scaling silicon photonic switch fabrics for data center interconnection networks. *Opt Express* **23**, 1159–1175 (2010).
7. Li, Y., Zhang, Y., Zhang, L. & Poon, A. W. Silicon and hybrid silicon photonic devices for intra-datacenter applications: state of the art and perspectives. *Photonics Res* **3**, B10–B27 (2015).
8. Shen, Y. *et al.* Deep learning with coherent nanophotonic circuits. *Nat Photonics* **11**, 441–446 (2017).
9. Tait, A. N. *et al.* Neuromorphic photonic networks using silicon photonic weight banks. *Sci Rep* **7**, 7430 (2017).
10. Shastri, B. J. *et al.* Photonics for artificial intelligence and neuromorphic computing. *Nat Photonics* **15**, 102–114 (2021).
11. Feldmann, J. *et al.* Parallel convolutional processing using an integrated photonic tensor core. *Nature* **589**, 52–58 (2021).
12. Huang, C. *et al.* A silicon photonic–electronic neural network for fibre nonlinearity compensation. *Nat Electron* **4**, 837–844 (2021).
13. Wang, J. *et al.* Chip-to-chip quantum photonic interconnect by path-polarization interconversion. *Optica* **3**, 407–413 (2016).
14. Qiang, X. *et al.* Large-scale silicon quantum photonics implementing arbitrary two-qubit processing. *Nat Photonics* **12**, 534–539 (2018).
15. Wang, J. *et al.* Multidimensional quantum entanglement with large-scale integrated optics. *Science (1979)* **360**, 285–291 (2018).
16. Llewellyn, D. *et al.* Chip-to-chip quantum teleportation and multi-photon entanglement in silicon. *Nat Phys* **16**, 148–153 (2020).
17. Arrazola, J. M. *et al.* Quantum circuits with many photons on a programmable nanophotonic chip. *Nature* **591**, 54–60 (2021).

18. Liu, W. *et al.* A fully reconfigurable photonic integrated signal processor. *Nat Photonics* **10**, 190–195 (2016).
19. Jouppi, N. *et al.* Tpu v4: An optically reconfigurable supercomputer for machine learning with hardware support for embeddings. in *Proceedings of the 50th Annual International Symposium on Computer Architecture* 1–14 (2023).
20. Pérez-López, D., López, A., DasMahapatra, P. & Capmany, J. Multipurpose self-configuration of programmable photonic circuits. *Nat Commun* **11**, 6359 (2020).
21. Ríos, C. *et al.* Integrated all-photonic non-volatile multi-level memory. *Nat Photonics* **9**, 725–732 (2015).
22. Zhang, Y. *et al.* Broadband transparent optical phase change materials for high-performance nonvolatile photonics. *Nat Commun* **10**, 4279 (2019).
23. Delaney, M., Zeimpekis, I., Lawson, D., Hewak, D. W. & Muskens, O. L. A New Family of Ultralow Loss Reversible Phase-Change Materials for Photonic Integrated Circuits: Sb<sub>2</sub>S<sub>3</sub> and Sb<sub>2</sub>Se<sub>3</sub>. *Adv Funct Mater* **30**, 2002447 (2020).
24. Ríos, C. *et al.* Ultra-compact nonvolatile phase shifter based on electrically reprogrammable transparent phase change materials. *Photonix* **3**, 26 (2022).
25. Yang, X. *et al.* Non-Volatile Optical Switch Element Enabled by Low-Loss Phase Change Material. *Adv Funct Mater* 2304601 (2023).
26. Xu, P., Zheng, J., Doylend, J. K. & Majumdar, A. Low-Loss and Broadband Nonvolatile Phase-Change Directional Coupler Switches. *ACS Photonics* **6**, 553–557 (2019).
27. Chen, R. *et al.* Broadband Nonvolatile Electrically Controlled Programmable Units in Silicon Photonics. *ACS Photonics* **9**, 2142–2150 (2022).
28. Stegmaier, M., Ríos, C., Bhaskaran, H., Wright, C. D. & Pernice, W. H. P. Nonvolatile All-Optical 1 × 2 Switch for Chipscale Photonic Networks. *Adv Opt Mater* **5**, 1600346 (2017).
29. Fang, Z. *et al.* Ultra-low-energy programmable non-volatile silicon photonics based on phase-change materials with graphene heaters. *Nat Nanotechnol* **17**, 842–848 (2022).
30. Liu, C., Maier, S. A. & Li, G. Genetic-algorithm-aided meta-atom multiplication for improved absorption and coloration in nanophotonics. *ACS Photonics* **7**, 1716–1722 (2020).
31. Ren, Y. *et al.* Genetic-algorithm-based deep neural networks for highly efficient photonic device design. *Photonics Res* **9**, B247–B252 (2021).
32. Felici, M., Atlasov, K. A., Surrente, A. & Kapon, E. Semianalytical approach to the design of photonic crystal cavities. *Phys Rev B* **82**, 115118 (2010).
33. Valagiannopoulos, C. & Lagoudakis, P. G. Photonic crystals for optimal color conversion in light-emitting diodes: a semi-analytical approach. *JOSA B* **35**, 1105–1112 (2018).
34. Piggott, A. Y. *et al.* Inverse design and demonstration of a compact and broadband on-chip wavelength demultiplexer. *Nat Photonics* **9**, 374–377 (2015).

35. Ahn, G. H. *et al.* Photonic inverse design of on-chip microresonators. *ACS Photonics* **9**, 1875–1881 (2022).
36. Molesky, S. *et al.* Inverse design in nanophotonics. *Nat Photonics* **12**, 659–670 (2018).
37. Jensen, J. S. & Sigmund, O. Topology optimization for nano-photonics. *Laser Photon Rev* **5**, 308–321 (2011).
38. Christiansen, R. E. & Sigmund, O. Inverse design in photonics by topology optimization: tutorial. *JOSA B* **38**, 496–509 (2021).
39. Delaney, M. *et al.* Nonvolatile programmable silicon photonics using an ultralow-loss Sb<sub>2</sub>Se<sub>3</sub> phase change material. *Sci Adv* **7**, eabg3500 (2021).
40. Wu, C. *et al.* Freeform direct-write and rewritable photonic integrated circuits in phase-change thin films. *Sci Adv* **10**, eadk1361 (2024).
41. Wang, Q. *et al.* Optically reconfigurable metasurfaces and photonic devices based on phase change materials. *Nat Photonics* **10**, 60–65 (2016).
42. Liu, H. *et al.* Rewritable color nanoprints in antimony trisulfide films. *Sci Adv* **6**, eabb7171 (2020).